scientific reports

Check for updates

OPEN

Skyrmion crystals in centrosymmetric itinerant magnets without horizontal mirror plane

Ryota Yambe[1,2]✉ & Satoru Hayami[2]

We theoretically investigate a new stabilization mechanism of a skyrmion crystal (SkX) in centrosymmetric itinerant magnets with magnetic anisotropy. By considering a trigonal crystal system without the horizontal mirror plane, we derive an effective spin model with an anisotropic Ruderman–Kittel–Kasuya–Yosida (RKKY) interaction for a multi-band periodic Anderson model. We find that the anisotropic RKKY interaction gives rise to two distinct SkXs with different skyrmion numbers of one and two depending on a magnetic field. We also clarify that a phase arising from the multiple-*Q* spin density waves becomes a control parameter for a field-induced topological phase transition between the SkXs. The mechanism will be useful not only for understanding the SkXs, such as that in Gd_2PdSi_3, but also for exploring further skyrmion-hosting materials in trigonal itinerant magnets.

A magnetic skyrmion, which is characterized by a topologically nontrivial spin texture[1–3], has been extensively studied in condensed matter physics since the discovery of the skyrmion crystal (SkX) in chiral magnets[4–6]. The SkX exhibits a nonzero topological winding number called the skyrmion number $N_{\rm sk}$, which is defined as $N_{\rm sk} = \sum_R \Omega_R/4\pi$, where Ω_R is a skyrmion density related to the solid angle consisting of three spins $\boldsymbol{S}_i$, $\boldsymbol{S}_j$, and $\boldsymbol{S}_k$ on the triangle R: $\tan(\Omega_R/2) = \boldsymbol{S}_i \cdot (\boldsymbol{S}_j \times \boldsymbol{S}_k)/(1 + \boldsymbol{S}_i \cdot \boldsymbol{S}_j + \boldsymbol{S}_j \cdot \boldsymbol{S}_k + \boldsymbol{S}_k \cdot \boldsymbol{S}_i)$[7]. The study of the SkX has attracted much attention, as the swirling topological magnetic texture owing to nonzero $N_{\rm sk}$ gives rise to an emergent electromagnetic field through the spin Berry phase and results in intriguing transport phenomena and dynamics[8–12], such as the topological Hall effect[13,14] and the skyrmion Hall effect[15,16].

The SkXs are expressed as a superposition of three spin density waves (triple-Q state) as

$$\boldsymbol{S}_i = \sum_{\eta=1}^{3} \left(\boldsymbol{e}_\eta \sin \mathcal{Q}'_{\eta i} + \boldsymbol{e}_z \cos \mathcal{Q}_{\eta i} \right), \tag{1}$$

where $\boldsymbol{e}_\eta$ and $\boldsymbol{e}_z$ are the unit vectors along the in-plane and z directions, respectively. $\mathcal{Q}_{\eta i} = \boldsymbol{Q}_\eta \cdot \boldsymbol{r}_i + \phi_\eta$, and $\mathcal{Q}'_{\eta i} = \mathcal{Q}_{\eta i} + \psi_\eta$ where ϕ_η and ψ_η are phases of each spin density wave. A variety of the SkXs are described by Eq. (1); a superposition of spiral waves for $\boldsymbol{e}_\eta \parallel \boldsymbol{e}_z \times \boldsymbol{Q}_\eta$ ($\boldsymbol{e}_\eta \parallel \boldsymbol{Q}_\eta$) and $\psi_1 = \psi_2 = \psi_3 = 0$ or π represents the Bloch-type (Néel-type) SkX, while that for $\psi_1 = \psi_2 = 0$ and $\psi_3 = \pi$ represents the anti-type SkX. The real-space spin texture for the Bloch-type SkX is shown in Fig. 1a. All the SkXs have the skyrmion number of one, $n_{\rm sk} \equiv |N_{\rm sk}| = 1$, in the magnetic unit cell and breaks the spatial inversion symmetry irrespective of $\boldsymbol{e}_\eta$ and ψ_η[8]. We call them the $n_{\rm sk} = 1$ SkXs. The $n_{\rm sk} = 1$ SkXs are stabilized by the Dzyaloshinskii-Moriya (DM) interaction[17,18] in chiral/polar magnets[4,19] or the competing exchange interactions in frustrated magnets[20–22].

Meanwhile, the spiral density waves are not necessarily for the formation of the SkX. By considering the superposition of the sinusoidal waves characterized by a different ψ_η, another type of the SkX can emerge, as shown in Fig. 1b[23,24]. In contrast to the $n_{\rm sk} = 1$ SkX, this spin texture exhibits the skyrmion number of two in a magnetic unit cell ($n_{\rm sk} = 2$ SkX), whose spatial inversion and/or sixfold rotational symmetries are broken depending on ϕ_η on a discrete lattice. For example, the $n_{\rm sk} = 2$ SkX with $\phi_\eta = \pi$ shown in Fig. 1b has the inversion symmetry, but the $n_{\rm sk} = 2$ SkX with $\phi_1 = 4\pi/3$, $\phi_2 = 2\pi/3$, and $\phi_3 = \pi$ shows the inversion symmetry breaking. Although the $n_{\rm sk} = 2$ SkX seems to be rare compared to the $n_{\rm sk} = 1$ one, it is stabilized by a multi-spin

[1]Department of Physics, Hokkaido University, Sapporo 060-0810, Japan. [2]Department of Applied Physics, The University of Tokyo, Tokyo 113-8656, Japan. ✉email: yambe@jphys.t.u-tokyo.ac.jp

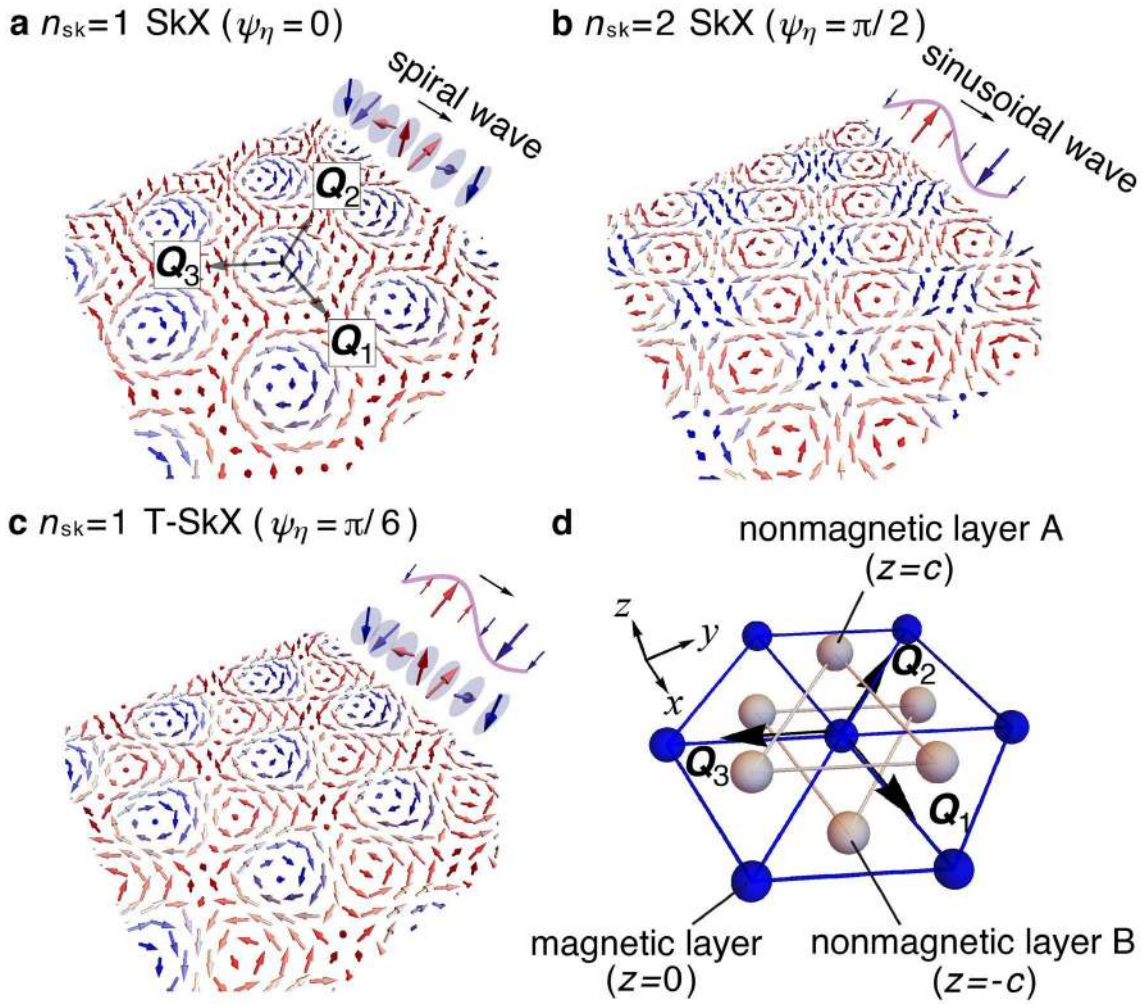

Figure 1. Schematic pictures of the SkXs and the crystal structure. (**a**–**c**) SkXs characterized by three spiral and sinusoidal waves along the $\boldsymbol{Q}_1$, $\boldsymbol{Q}_2$, and $\boldsymbol{Q}_3$ directions: (**a**) the $n_{sk} = 1$ SkX for $\psi_\eta = 0$, (**b**) the $n_{sk} = 2$ SkX for $\psi_\eta = \pi/2$, and (**c**) the $n_{sk} = 1$ T-SkX for $\psi_\eta = \pi/6$ in Eq. (1). (**d**) Centrosymmetric trigonal structure without the horizontal mirror plane. The blue spheres represent magnetic sites, while the gray spheres shifted by $+c$ $(-c)$ from the center of the downward (upward) triangles on the magnetic layer represent nonmagnetic sites on a layer A (B).

interaction in itinerant magnets [23,24] or an anisotropic symmetric exchange interaction in frustrated magnets[25]. Moreover, an isolated skyrmion with $n_{sk} = 2$ is nucleated in frustrated magnets[26,27].

In the present study, we report our theoretical discovery of the SkXs by focusing on a magnetic anisotropy that arises from the absence of the mirror symmetry in the crystal structure. By constructing a microscopic effective spin model and performing simulated annealing for triangular itinerant magnets, we show that an anisotropic Ruderman–Kittel–Kasuya–Yosida (RKKY) interaction [28–30] arising from the absence of the mirror symmetry on a magnetic layer [Fig. 1d] induces the SkXs with $n_{sk} = 1$ and $n_{sk} = 2$. The anisotropic RKKY interaction stabilizes the SkXs even without the DM, competing exchange, and multi-spin interactions[25,31–35]. The obtained SkXs exhibit different symmetry breaking compared to that found in previous studies[4,19]. The spin texture in the SkX with $n_{sk} = 1$ does not have the sixfold rotational symmetry in addition to the inversion symmetry, as shown in Fig. 1c, which is different from that in chiral and frustrated magnets in Fig. 1a. We here call this state the $n_{sk} = 1$ threefold-rotational-symmetric SkX (T-SkX). Meanwhile, the $n_{sk} = 2$ SkX shows the inversion symmetry breaking. Furthermore, we elucidate that topological phase transitions between the $n_{sk} = 1$ T-SkX, the $n_{sk} = 2$ SkX, and another non-topological triple-Q state are caused by a change with respect to the relative phase ψ_η in Eq. (1), which is controlled by the degree of the mirror symmetry breaking. This mechanism for the SkXs might be useful to understand a microscopic origin of the SkX in Gd_2PdSi_3[36–38], as the underlying lattice structure without the mirror plane on a magnetic layer is common[39].

Results

Model. Let us start by showing an effective spin model starting from a multi-band periodic Anderson model consisting of localized and itinerant electrons. To trace out the itinerant electron degree of freedom and obtain effective magnetic interactions between localized spins, we adopt the standard Schrieffer-Wolff transformation[40]

and perform the perturbative expansion of the grand potential with respect to the anisotropic spin-charge coupling[24,41], as detailed in Supplementary Information. Generally, the effective spin model is given by

$$\mathcal{H} = -2\sum_{\eta}\left[J_{\boldsymbol{Q}_\eta}\boldsymbol{S}_{\boldsymbol{Q}_\eta}\cdot\boldsymbol{S}_{-\boldsymbol{Q}_\eta} + \sum_{\alpha\beta}K^{\alpha\beta}_{\boldsymbol{Q}_\eta}S^{\alpha}_{\boldsymbol{Q}_\eta}S^{\beta}_{-\boldsymbol{Q}_\eta} + i\boldsymbol{D}_{\boldsymbol{Q}_\eta}\cdot\left(\boldsymbol{S}_{\boldsymbol{Q}_\eta}\times\boldsymbol{S}_{-\boldsymbol{Q}_\eta}\right)\right], \tag{2}$$

where $\alpha,\beta = x,y,z$, $\boldsymbol{S}_{\boldsymbol{Q}_\eta}$ is the Fourier transform of the localized electron spin $\boldsymbol{S}_i$ at site i ($|\boldsymbol{S}_i| = 1$), and the coefficient 2 arises from the $-\boldsymbol{Q}_\eta$ contribution. The effective spin model consists of an isotropic RKKY interaction, symmetric anisotropic RKKY interaction, and antisymmetric DM-type RKKY interaction with coupling constants $J_{\boldsymbol{Q}_\eta}$, $K^{\alpha\beta}_{\boldsymbol{Q}_\eta}$, and $D^{\alpha}_{\boldsymbol{Q}_\eta}$, respectively. The coupling constants are defined by

$$J_{\boldsymbol{Q}_\eta} = \frac{1}{3}\sum_{\alpha}\chi^{\alpha\alpha}_{\boldsymbol{Q}_\eta}, \tag{3}$$

$$K^{\alpha\beta}_{\boldsymbol{Q}_\eta} = \mathrm{Re}\left[\chi^{\alpha\beta}_{\boldsymbol{Q}_\eta}\right] - \mathrm{J}_{\boldsymbol{Q}_\eta}\delta_{\alpha\beta}, \tag{4}$$

$$D^{\alpha}_{\boldsymbol{Q}_\eta} = \sum_{\beta\gamma}\frac{\epsilon_{\alpha\beta\gamma}}{2}\mathrm{Im}\left[\chi^{\beta\gamma}_{\boldsymbol{Q}_\eta}\right], \tag{5}$$

where $\chi^{\alpha\beta}_{\boldsymbol{q}}$ corresponds to the bare susceptibility of itinerant electrons, $\delta_{\alpha\beta}$ is the Kronecker delta, and $\epsilon_{\alpha\beta\gamma}$ is the Levi-Civita symbol. In Eq. (2), the wave vector $\boldsymbol{Q}_\eta$ is chosen by supposing that $\chi_{\boldsymbol{Q}_\eta} > \chi_{\boldsymbol{q}}$, which is relevant to the lattice symmetry. The anisotropic interactions, $K^{\alpha\beta}_{\boldsymbol{Q}_\eta}$, and $D^{\alpha}_{\boldsymbol{Q}_\eta}$, originate from the atomic spin-orbit coupling[42–44]. The number of $\boldsymbol{Q}_\eta$ and nonzero components of the interactions are determined by the lattice symmetry.

For the above effective spin model, we consider the lattice structure in Fig. 1d consisting of a magnetic layer sandwiched by two nonmagnetic layers. The nonmagnetic ions at $z = c$ ($z = -c$) are located above (below) the downward (upward) triangles on the magnetic layer at $z = 0$, which breaks the horizontal mirror symmetry at $z = 0$ while keeping the inversion symmetry. The lattice symmetry is compatible with the $D_{3\mathrm{d}}$ point group symmetry. In this situation, we set three $\boldsymbol{Q}_\eta$ and four independent coupling constants to satisfy the $D_{3\mathrm{d}}$ symmetry. The former is given by $\boldsymbol{Q}_1 = (2\pi/6, 0, 0)$, $\boldsymbol{Q}_2 = (-\pi/6, \sqrt{3}\pi/6, 0)$, and $\boldsymbol{Q}_3 = (-\pi/6, -\sqrt{3}\pi/6, 0)$ and the latter is given by $J_{\boldsymbol{Q}_1}$, $K^{xx}_{\boldsymbol{Q}_1}$, $K^{yy}_{\boldsymbol{Q}_1}$, and $K^{yz}_{\boldsymbol{Q}_1}$: $J_{\boldsymbol{Q}_1} = J_{\boldsymbol{Q}_2} = J_{\boldsymbol{Q}_3}$, $K^{xx}_{\boldsymbol{Q}_2} = K^{xx}_{\boldsymbol{Q}_3} = (K^{xx}_{\boldsymbol{Q}_1} + 3K^{yy}_{\boldsymbol{Q}_1})/4$, $K^{yy}_{\boldsymbol{Q}_2} = K^{yy}_{\boldsymbol{Q}_3} = (3K^{xx}_{\boldsymbol{Q}_1} + K^{yy}_{\boldsymbol{Q}_1})/4$, $K^{zz}_{\boldsymbol{Q}_1} = K^{zz}_{\boldsymbol{Q}_2} = K^{zz}_{\boldsymbol{Q}_3} = -K^{xx}_{\boldsymbol{Q}_1} - K^{yy}_{\boldsymbol{Q}_1}$, $-K^{xy}_{\boldsymbol{Q}_2} = -K^{yx}_{\boldsymbol{Q}_2} = K^{xy}_{\boldsymbol{Q}_3} = K^{yx}_{\boldsymbol{Q}_3} = \sqrt{3}(K^{xx}_{\boldsymbol{Q}_1} - K^{yy}_{\boldsymbol{Q}_1})/4$, $K^{yz}_{\boldsymbol{Q}_1} = K^{zy}_{\boldsymbol{Q}_1} = -2K^{xz}_{\boldsymbol{Q}_2}/\sqrt{3} = -2K^{zx}_{\boldsymbol{Q}_2}/\sqrt{3} = -2K^{yz}_{\boldsymbol{Q}_2} = -2K^{zy}_{\boldsymbol{Q}_2} = 2K^{xz}_{\boldsymbol{Q}_3}/\sqrt{3} = 2K^{zx}_{\boldsymbol{Q}_3}/\sqrt{3} = -2K^{yz}_{\boldsymbol{Q}_3} = -2K^{zy}_{\boldsymbol{Q}_3}$ (all other coupling constants are zero). Among three anisotropic coupling constants, we focus on the effect of $K^{yz}_{\boldsymbol{Q}_1}$, which originates from the horizontal mirror symmetry breaking and is characteristic of the $D_{3\mathrm{d}}$ symmetry, on the stabilization of the multiple-Q states, and $K^{xx}_{\boldsymbol{Q}_1}$ and $K^{yy}_{\boldsymbol{Q}_1}$ are neglected for simplicity[31,34]. In the end, the effective spin model is summarized as

$$\mathcal{H} = -2\sum_{\eta=1}^{3}\left(J\boldsymbol{S}_{\boldsymbol{Q}_\eta}\cdot\boldsymbol{S}_{-\boldsymbol{Q}_\eta} + \Gamma\sum_{\alpha\beta}I^{\alpha\beta}_{\boldsymbol{Q}_\eta}S^{\alpha}_{\boldsymbol{Q}_\eta}S^{\beta}_{-\boldsymbol{Q}_\eta}\right) - H\sum_{i}S^{z}_{i}. \tag{6}$$

Here, $J \equiv J_{\boldsymbol{Q}_1}$, $\Gamma \equiv K^{yz}_{\boldsymbol{Q}_1}$, $I^{yz}_{\boldsymbol{Q}_1}$=$I^{zy}_{\boldsymbol{Q}_1}$=1, $I^{yz}_{\boldsymbol{Q}_2}$=$I^{zy}_{\boldsymbol{Q}_2}$=−1/2, $I^{xz}_{\boldsymbol{Q}_2}$=$I^{zx}_{\boldsymbol{Q}_2}$=$-\sqrt{3}$/2, $I^{yz}_{\boldsymbol{Q}_3}$=$I^{zy}_{\boldsymbol{Q}_3}$=−1/2, and $I^{xz}_{\boldsymbol{Q}_3}$=$I^{zx}_{\boldsymbol{Q}_3}$=$\sqrt{3}$/2 (all other component of $I_{\boldsymbol{Q}_\eta}$ are zero). The symmetric aniostropic interaction with Γ is qualitatively different from the antisymmetric DM interaction: the former can appear irrespective of the inversion symmetry, while the latter requires the inversion symmetry breaking, and thus vanishes in Eq. (6). The Γ term also appears in the other trigonal crystal systems. We also introduce the Zeeman coupling to an external magnetic field H along the z direction.

Magnetic phase diagram. A magnetic phase diagram of the model in Eq. (6) is calculated by simulated annealing combined with the standard Metropolis local updates. Figure 2a shows the magnetic phase diagram while changing Γ and H in the unit of J at a temperature of 0.01. To identify magnetic phases, we compute the magnetization $M = (1/N)\sum_j\langle S^z_j\rangle$ and the spin structure factor $S^{\alpha\alpha}_s(\boldsymbol{q}) = (1/N)\sum_{jl}\langle S^{\alpha}_j S^{\alpha}_l\rangle e^{i\boldsymbol{q}\cdot(\boldsymbol{r}_j-\boldsymbol{r}_l)}$, where $\boldsymbol{r}_j$ is the position vector at site j, $N = 48^2$ is the system size, and $\langle\cdots\rangle$ is the thermal average. We also calculate the spin scalar chirality $\chi_{\mathrm{sc}} = (1/N)\sum_R\langle[\boldsymbol{S}_i\cdot(\boldsymbol{S}_j\times\boldsymbol{S}_k)]_R\rangle$ where the subscript R represents the center of the triangle and i, j and k are in the counterclockwise order. We obtain six different magnetic phases besides the single-Q (1Q) conical state for $\Gamma = 0$ and the fully-polarized (FP) state for $H \gtrsim 2$, whose real-space spin configurations and the in-(out-of-)plane spin structure factor $S^{\perp}_s(\boldsymbol{q}) = S^{xx}_s(\boldsymbol{q}) + S^{yy}_s(\boldsymbol{q})$ [$S^{zz}_s(\boldsymbol{q})$] are shown in Fig. 2b–g. We also show the skyrmion density Ω_R for each spin configuration in Fig. 2h–m.

For $\Gamma = 0$, the model in Eq. (6) reduces to the isotropic RKKY model, which stabilizes the 1Q conical state for any H. By introducing Γ, the multiple-Q instabilities occur: the triple-Q I (3Q-I) state is stabilized for small H, while the triple-Q II (3Q-II) state is stabilized for large H, as shown in Fig. 2a. Their spin modulations are mainly characterized by the in-plane single-q component, which smoothly connects to the 1Q conical state.

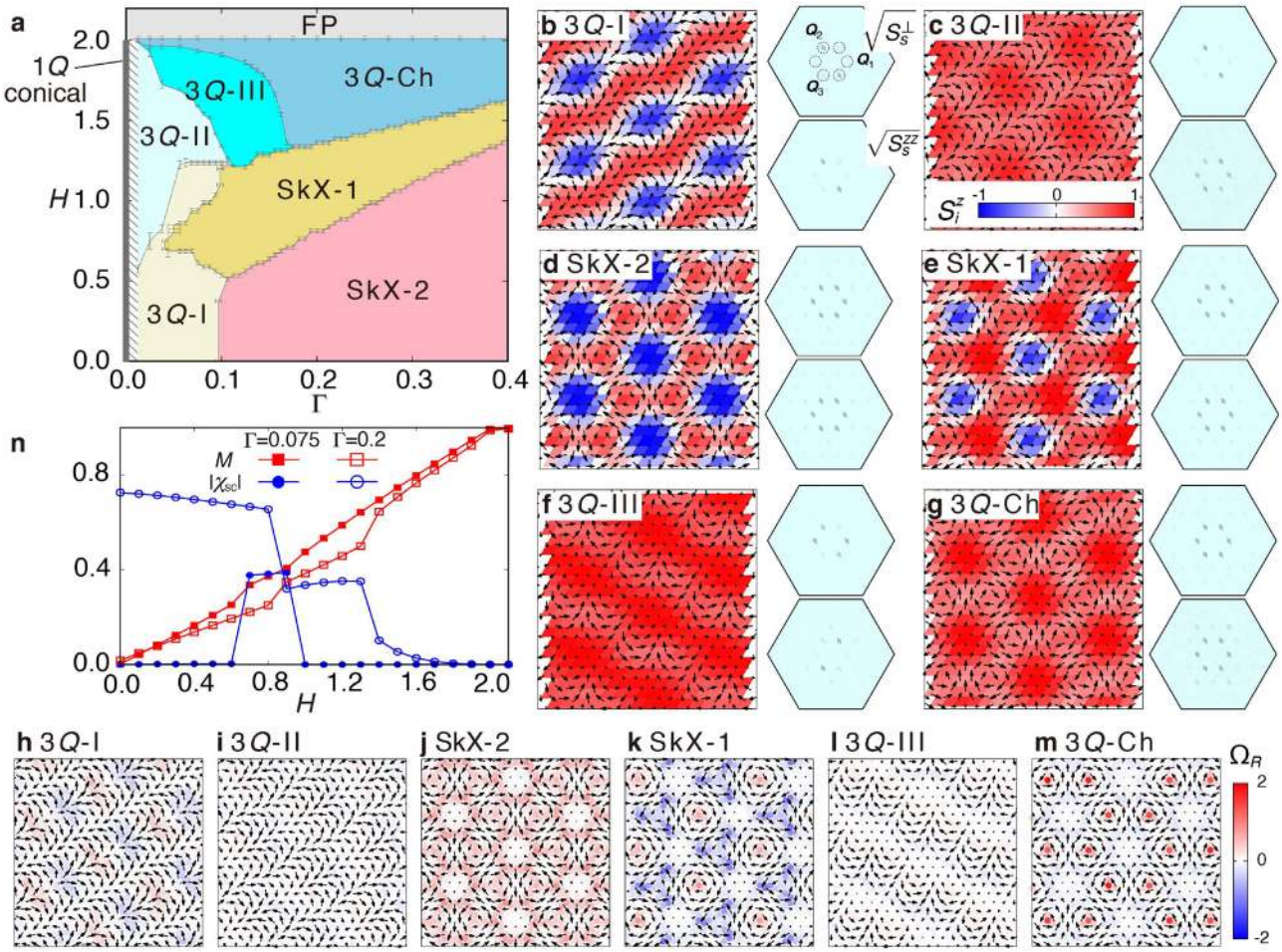

Figure 2. Magnetic phase diagram and characteristics of magnetic phases. (**a**) Γ-H magnetic phase diagram for the model in Eq. (6) in the unit of J. The 3Q-I, 3Q-II, 3Q-III, SkX-2, SkX-1, 3Q-Ch, 1Q conical, and FP represent the triple-Q I, triple-Q II, triple-Q III, $n_{\rm sk} = 2$ SkX, $n_{\rm sk} = 1$ T-SkX, triple-Q chiral, single-Q conical, and fully polarized states, respectively. In the hatched region, energies for several magnetic states are degenerate and it is difficult to determine the phase boundaries. (**b**–**g**) Snapshots of the spin configurations in (**b**) 3Q-I for $\Gamma = 0.075$ and $H = 0.4$, (**c**) 3Q-II for $\Gamma = 0.075$ and $H = 1.3$, (**d**) SkX-2 for $\Gamma = 0.2$ and $H = 0$, (**e**) SkX-1 for $\Gamma = 0.2$ and $H = 1$, (**f**) 3Q-III for $\Gamma = 0.075$ and $H = 1.6$, and (**g**) 3Q-Ch for $\Gamma = 0.2$ and $H = 1.4$. The arrows and contour denote the xy and z components of the spin moments, respectively. The square root of in-plane and out-of-plane spin structure factors in the Brillouin zone are shown in upper and lower panels, respectively, where the dashed circles highlight $\pm\boldsymbol{Q}_1$, $\pm\boldsymbol{Q}_2$, and $\pm\boldsymbol{Q}_3$ and the $\boldsymbol{q} = 0$ component is removed for better visibility. (**h**–**m**) Real-space distributions of the skyrmion density Ω_R for the spin configurations in (**b**–**g**), respectively. (**n**) H dependences of the magnetization (red square) and spin scalar chirality (blue circle) for $\Gamma = 0.075$ (filled symbols) and $\Gamma = 0.2$ (open symbols).

Meanwhile, they exhibit different peak structures in $S^{zz}_s(\boldsymbol{q})$, as shown in Fig. 2b,c: there is a dominant peak at $\boldsymbol{Q}_2$ in the 3Q-I state, whereas there are two dominant peaks at $\boldsymbol{Q}_1$ and $\boldsymbol{Q}_3$ in the 3Q-II state in addition to the peak at $\boldsymbol{Q}_2$ in $S^{\perp}_s(\boldsymbol{q})$. Both phases are topologically trivial without $\chi_{\rm sc}$.

While increasing Γ, the 3Q-I state is replaced by the $n_{\rm sk} = 2$ SkX (SkX-2) in the low-field region for $\Gamma \gtrsim 0.1$ and the $n_{\rm sk} = 1$ T-SkX (SkX-1) in the intermediate-field region for $\Gamma \gtrsim 0.05$, as shown in Fig. 2a. Both SkXs are characterized by the triple-Q peaks with the same intensities, as shown in Fig. 2d,e. By looking into the real-space spin configurations, they are formed by a vortex with vorticity $\nu = -2$ and two vortices with $\nu = +1$ in a magnetic unit cell in Fig. 2d,e, which indicates the inversion symmetry breaking. The positions at the cores with negative S^z_i are different with each other. They are located at the cores with $\nu = -2$ ($\nu = +1$) for the $n_{\rm sk} = 2$ SkX ($n_{\rm sk} = 1$ T-SkX). Such a difference results in the different skyrmion numbers, which is clearly found in Fig. 2j,k.

In the high-field region, the 3Q-II state and $n_{\rm sk} = 1$ T-SkX are replaced by the other topologically trivial triple-Q states depending on Γ: the triple-Q III (3Q-III) or the triple-Q chiral (3Q-Ch) state. The 3Q-III state is mainly characterized by the in-plane double-Q peaks in Fig. 2f, while the 3Q-Ch state is by the in-plane triple-Q peaks with equal intensities in Fig. 2g. The 3Q-Ch state exhibits nonzero $\chi_{\rm sc}$, although the skyrmion number becomes zero.

We show H dependences of M and $|\chi_{\rm sc}|$ for $\Gamma = 0.075$ and 0.2 in Fig. 2n. While increasing H, jumps of M and $\chi_{\rm sc}$ appear when the skyrmion number changes: Two jumps between the $n_{\rm sk} = 1$ T-SkX and the 3Q-I are found

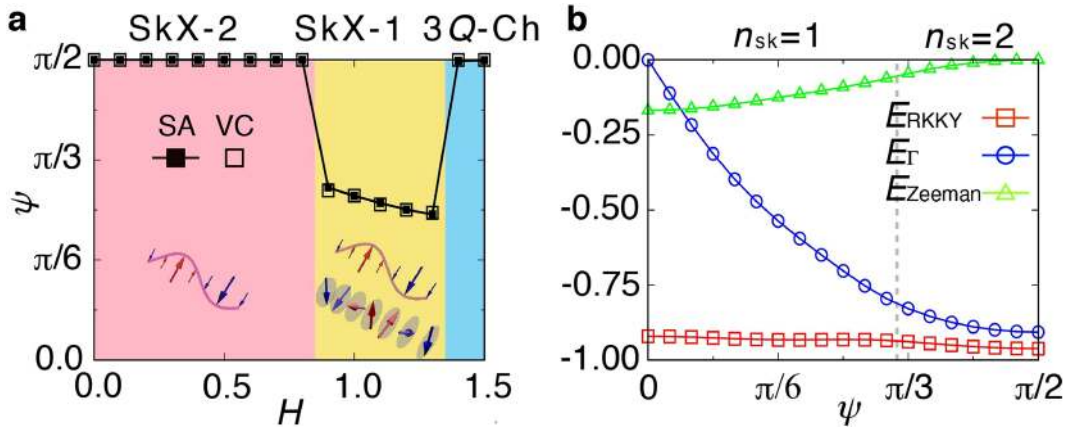

Figure 3. Mechanism of the topological transition for $\Gamma \gtrsim 0.2$. (**a**) H dependence of the phase ψ obtained from the simulated annealing (SA) and variational calculation (VC) in the model in Eq. (6) at $\Gamma = 0.2$. Schematic pictures of the constitute waves in each SkX are shown in the inset. (**b**) ψ dependences of energies from different contributions, $E_{\rm RKKY}$, E_Γ, and $E_{\rm Zeeman}$ in the unit of J, Γ, and H, respectively, for $A = 1/\sqrt{2}$, $m_z = 0$, $\phi_1 = 4\pi/3$, $\phi_2 = 2\pi/3$, and $\phi_3 = \pi$ in Eq. (7) with $|\boldsymbol{S}_i| = 1$. The vertical dashed line represents the boundary between the SkXs with $n_{\rm sk} = 1$ and 2.

at $H \simeq 0.7$ and $\simeq 0.9$ for $\Gamma = 0.075$ and other two jumps are found between the $n_{\rm sk} = 2$ SkX and the $n_{\rm sk} = 1$ T-SkX and between the $n_{\rm sk} = 1$ T-SkX and the 3Q-Ch for $\Gamma = 0.2$. The transition between the $n_{\rm sk} = 1$ T-SkX and the 3Q-III for $0.1 < \Gamma < 0.17$ also shows jumps of M and $\chi_{\rm sc}$.

Mechanism of the topological transition. Next, we show the transformation of the skyrmion numbers on the basis of the phase degrees of freedom among the constituent triple-Q density waves. We find that the spin configurations for the $n_{\rm sk} = 1$ T-SkX in Fig. 2e and $n_{\rm sk} = 2$ SkX in Fig. 2d are summarized in a single expression as

$$\boldsymbol{S}_i \propto \begin{pmatrix} -\frac{\sqrt{3}}{2}\sin\mathcal{Q}'_{2i} + \frac{\sqrt{3}}{2}\sin\mathcal{Q}'_{3i} \\ \sin\mathcal{Q}'_{1i} - \frac{1}{2}\sin\mathcal{Q}'_{2i} - \frac{1}{2}\sin\mathcal{Q}'_{3i} \\ A(\cos\mathcal{Q}_{1i} + \cos\mathcal{Q}_{2i} + \cos\mathcal{Q}_{3i}) + m_z \end{pmatrix}^T, \tag{7}$$

where A and m_z are additional variational parameters compared to Eq. (1), and we set $\boldsymbol{e}_\eta \parallel \boldsymbol{e}_z \times \boldsymbol{Q}_\eta$ and $\psi \equiv \psi_1 = \psi_2 = \psi_3$ for $\Gamma > 0$. There are two types of phase degrees of freedom in Eq. (7). One is a phase among the constituent waves, ϕ_η, which induces the transformation between the SkX and the vortex crystal with staggered spin scalar chirality[45]. The other is a relative phase between in-plane- and z-spin components, ψ, which induces the different types of the SkX, as discussed in the introduction: the $n_{\rm sk} = 1$ T-SkX for $0 < \psi < \psi_{\rm c}$ and $n_{\rm sk} = 2$ SkX for $\psi_{\rm c} \le \psi \le \pi/2$, where $\psi_{\rm c}$ depends on the other variational parameters. From the symmetry viewpoint, nonzero ψ in the $n_{\rm sk} = 2$ SkX and $n_{\rm sk} = 1$ T-SkX shows the sixfold-rotational symmetry breaking in addition to the inversion symmetry breaking, which is in contrast to $\psi = 0$ in the $n_{\rm sk} = 1$ SkX in chiral magnets.

The phase diagram obtained by the simulated annealing in Fig. 2a is well reproduced by the variational spin ansatz in Eq. (7) for $\Gamma \gtrsim 0.2$. This means that ψ is evaluated through the spin ansatz in Eq. (7). Figure 3a shows H dependence of ψ by simulated annealing and variational calculation at $\Gamma = 0.2$. Both the results show that the $n_{\rm sk} = 2$ SkX exhibits $\psi = 0.5\pi$, the $n_{\rm sk} = 1$ T-SkX exhibits $0.24\pi \lesssim \psi \lesssim 0.3\pi$, and the 3$Q$-Ch exhibits $\psi = 0.5\pi$. Thus, the phase transitions among the $n_{\rm sk} = 2$ SkX, the $n_{\rm sk} = 1$ T-SkX, and the 3Q-Ch are regarded as the phase transitions with respect to ψ. In other words, the topological transitions are caused by the changes of the types of constitute waves, as shown in Fig. 3a.

The phase transition characterized by the change of ψ is due to the mirror symmetry breaking in the lattice structure. To demonstrate that, we calculate the energy contributions from each term in the model in Eq. (6): the RKKY energy $E_{\rm RKKY} = -2J\sum_\eta \boldsymbol{S}_{\boldsymbol{Q}_\eta} \cdot \boldsymbol{S}_{-\boldsymbol{Q}_\eta}/N$, the anisotropic energy $E_\Gamma = -2\Gamma\sum_{\eta\alpha\beta} I^{\alpha\beta}_{\boldsymbol{Q}_\eta} S^\alpha_{\boldsymbol{Q}_\eta} S^\beta_{-\boldsymbol{Q}_\eta}/N$, and the Zeeman energy $E_{\rm Zeeman} = -H\sum_i S^z_i/N$. Figure 3b shows ψ dependences of $E_{\rm RKKY}$, E_Γ, and $E_{\rm Zeeman}$ for the spin ansatz in Eq. (7) with $|\boldsymbol{S}_i| = 1$ at fixed $A = 1/\sqrt{2}$, $m_z = 0$, $\phi_1 = 4\pi/3$, $\phi_2 = 2\pi/3$, and $\phi_3 = \pi$, where ψ_c is around $\pi/3$. $E_{\rm RKKY}$ has little ψ dependence, whereas E_Γ and $E_{\rm Zeeman}$ show distinct behaviors against ψ; E_Γ ($E_{\rm Zeeman}$) decreases while increasing (decreasing) ψ. In other words, Γ arising from the mirror symmetry breaking tends to favor the $n_{\rm sk} = 2$ SkX with $\psi = \pi/2$, while the magnetic field tends to favor the $n_{\rm sk} = 1$ SkX with $\psi = 0$. The competition between these distinct behaviors causes the filed-induced transition from the $n_{\rm sk} = 2$ SkX to the $n_{\rm sk} = 1$ T-SkX with $0.24\pi \lesssim \psi \lesssim 0.3\pi$.

Summary

In conclusion, we clarify that the magnetic anisotropy arising from the breaking of the mirror symmetry is another way to stabilize the SkXs in itinerant magnets irrespective of the spatial inversion symmetry. On the basis of simulated annealing and variational calculation, we show that the anisotropic RKKY interaction induces two SkXs with different topological numbers, which accompanies the spontaneous inversion symmetry breaking. Moreover, we find that two SkXs are transformed with each other by changing the anisotropic RKKY interaction and magnetic field, the former of which is tuned by the degree of mirror symmetry breaking.

Our study reveals that the $n_{\rm sk} = 1$ and $n_{\rm sk} = 2$ SkXs are stabilized even without the multi-spin interaction in itinerant magnets, which is distinct from the previous one in the Kondo lattice model without the magnetic anisotropy[23]: The anisotropic bilinear exchange interaction plays an important role in the stabilization of the former SkXs, while the isotropic biquadratic interaction is important for the latter one[24]. Although both the systems exhibit similar skyrmion textures, the degeneracy in terms of the vorticity and helicity is different owing to the different mechanisms. The SkXs by the isotropic biquadratic interaction are energetically degenerate for different vorticity and helicity, while the present SkXs have a definite vorticity and helicity depending on the sign of the anisotropic interaction. Reflecting such a difference, the SkXs in the present model induce a different Goldstone mode from that in the previous model, which results in different dynamics. Furthermore, the anisotropic response against the electromagnetic field is anticipated due to the nature of magnetic anisotropy, which might give rise to further unconventional multiple-Q states. Such a theoretical exploration of the SkXs based on magnetic anisotropy will be left for future study.

Finally, let us discuss a relevant material in the present mechanism. The centrosymmetric itinerant magnet Gd_2PdSi_3[36] might be a candidate material, which hosts the skyrmion crystal in an external magnetic field. The importance of the RKKY interaction from the nesting of the Fermi surfaces has already been suggested by the angle-resolved photoemission spectroscopy[46,47]. In addition, the anisotropic RKKY interaction would play an important role in this compound, as the magnetic Gd ions form the triangular lattice and they are sandwiched by the nonmagnetic Pd and Si so that the mirror symmetry on each magnetic layer is broken[39,48]. Indeed, the importance of the multi-orbital degrees of freedom, which become the microscopic origin of the anisotropic RKKY interaction, has also been implied by first-principle calculations[46,49]. It would be interesting to test our scenario for the SkX in Gd_2PdSi_3 by considering the superstructure of the Pd and Si and the effect of the spin-orbit coupling. Our mechanism will also shed light on engineering the SkXs in quasi-two-dimensional magnetic materials including surface, domain, and layered systems.

Methods

Simulated annealing. We perform the simulated annealing combined with the standard Metropolis local updates under the periodic boundary condition. In the simulation, we gradually reduce the temperature with a rate $T_{n+1} = \alpha T_n$, where T_n is the temperature at the nth step. We set the initial temperature $T_0 = 1$ and the coefficient $\alpha = 0.99954$. The final temperature $T \simeq 0.01$ is reached after total 10^6 steps, where we perform 10^2 Monte Carlo sweeps at each temperature. At the final temperature, we perform 10^6 Monte Carlo sweeps for thermalization and measurements, respectively. Although Figs. 2 and 3a show the results for $N = 48^2$, we confirm that the obtained result does not change for $N = 96^2$. We also confirm that the simulations with different values of α, $\alpha = 0.99908, 0.99541$, and 0.95499, give the same result.

Variational calculation. We here present the details of the spin ansatz in Eq. (7) and the variational calculation. To find the spin configuration in Eq. (7), we start from a general spin ansatz of the single-Q spiral state given by

$$\boldsymbol{S}_i^{\eta} = \tilde{\boldsymbol{e}}_{\eta y} b \sin \mathcal{Q}''_{\eta i} + \tilde{\boldsymbol{e}}_{\eta z} a \cos \mathcal{Q}''_{\eta i}, \tag{8}$$

where $\mathcal{Q}''_{\eta i} = \boldsymbol{Q}_{\eta} \cdot \boldsymbol{r}_i + \varphi_{\eta}, \tilde{\boldsymbol{e}}_{\eta y} = \boldsymbol{e}_{\eta} \cos\theta - \boldsymbol{e}_z \sin\theta$, and $\tilde{\boldsymbol{e}}_{\eta z} = \boldsymbol{e}_{\eta} \sin\theta + \boldsymbol{e}_z \cos\theta \, (0 \le \theta < \pi)$. This spin configuration expresses an elliptical wave, where the axis with a length of $2a$ is parallel to $\tilde{\boldsymbol{e}}_{\eta z}$ and the axis with a length of $2b$ $(a > b \ge 0)$ is parallel to $\tilde{\boldsymbol{e}}_{\eta y}$. The spin ansatz in Eq. (8) describes a variety of spin density waves depending on $r \equiv b/a$ and θ: the spiral wave ($r = 1$), standard elliptical wave ($0 < r < 1$ and $\theta = 0, \pi/2$), rotated elliptical wave ($0 < r < 1$ and $\theta \neq 0, \pi/2$), standard sinusoidal wave ($r = 0$ and $\theta = 0, \pi/2$), and rotated sinusoidal wave ($r = 0$ and $\theta \neq 0, \pi/2$), where "standard" means that the axes are parallel to $\boldsymbol{e}_{\eta}$ or $\boldsymbol{e}_z$. A schematic picture of spiral plane in Eq. (8) is shown in Supplementary Information.

We rewrite the spin configuration in Eq. (8) as

$$\boldsymbol{S}_i^{\eta} = \boldsymbol{e}_{\eta} A_{\perp} \sin(\mathcal{Q}''_{\eta i} + \Theta_{\perp}) + \boldsymbol{e}_z A_z \cos(\mathcal{Q}''_{\eta i} + \Theta_z), \tag{9}$$

where $\Theta_{\perp}$, Θ_z, A_z, and $A_{\perp}$ satisfy $\tan\Theta_{\perp} = \tan\theta/r$, $\tan\Theta_z = r\tan\theta$, $A_{\perp} = \sqrt{a^2\sin^2\theta + b^2\cos^2\theta}$, and $A_z = \sqrt{a^2\cos^2\theta + b^2\sin^2\theta}$, respectively. Then, the spin ansatz in Eq. (7) is obtained by superposing three spin density waves in Eq. (9) in addition to a uniform z component, which is given by

$$\boldsymbol{S}_i \propto \sum_{\eta} \boldsymbol{S}_i^{\eta} + M_z \boldsymbol{e}_z. \tag{10}$$

The variational parameters A, m_z, ϕ_{η}, and ψ_{η} in Eq. (7) are related to that in Eq. (10) as $A = A_z/A_{\perp}$, $m_z = M_z/A_{\perp}$ $\phi_{\eta} = \varphi_{\eta} + \Theta_z$ and $\psi_{\eta} = \Theta_{\perp} - \Theta_z$. From the definition, ψ_{η} does not depend on η, i.e., $\psi_1 = \psi_2 = \psi_3 \equiv \psi$.

In the variational calculations in Fig. 3a, we optimize a, b, θ, φ_η, and M_z as the variational parameters for $N = 12^2$. After obtaining the optimal parameters, we calculate ψ in Fig. 3a from the difference between phases of $S^y_{\mathbf{Q}_1}$ and $S^z_{\mathbf{Q}_1}$. In Supplementary Information, we show H dependences of the magnetic moment, magnetization, and spin scalar chirality by the variational calculation and the simulated annealing. Compared to the results, one can find that the variational spin ansatz in Eq. (7) corresponds to the spin textures obtained by the simulated annealing.

Data availibility

The datasets generated during and/or analysed during the current study are available from the corresponding author on reasonable request.

Received: 21 February 2021; Accepted: 10 May 2021
Published online: 27 May 2021

References

1. Skyrme, T. H. R. A unified field theory of mesons and baryons. *Nucl. Phys.* **31**, 556–569. https://doi.org/10.1016/0029-5582(62)90775-7 (1962).
2. Bogdanov, A. N. & Yablonskii, D. A. Thermodynamically stable "vortices" in magnetically ordered crystals: The mixed state of magnets. *Sov. Phys. JETP* **68**, 101–103 (1989).
3. Bogdanov, A. & Hubert, A. Thermodynamically stable magnetic vortex states in magnetic crystals. *J. Magn. Magn. Mater.* **138**, 255–269. https://doi.org/10.1016/0304-8853(94)90046-9 (1994).
4. Rößler, U. K., Bogdanov, A. N. & Pfleiderer, C. Spontaneous skyrmion ground states in magnetic metals. *Nature* **442**, 797–801. https://doi.org/10.1038/nature05056 (2006).
5. Mühlbauer, S. *et al.* Skyrmion lattice in a chiral magnet. *Science* **323**, 915–919. https://doi.org/10.1126/science.1166767 (2009).
6. Yu, X. Z. *et al.* Real-space observation of a two-dimensional skyrmion crystal. *Nature* **465**, 901–904. https://doi.org/10.1038/nature09124 (2010).
7. Berg, B. & Lübcscher, M. Definition and statistical distributions of a topological number in the lattice o(3) σ-model. *Nucl. Phys. B* **190**, 412–424. https://doi.org/10.1016/0550-3213(81)90568-X (1981).
8. Nagaosa, N. & Tokura, Y. Topological properties and dynamics of magnetic skyrmions. *Nat. Nanotechnol.* **8**, 899–911. https://doi.org/10.1038/nnano.2013.243 (2013).
9. Fert, A., Reyren, N. & Cros, V. Magnetic skyrmions: Advances in physics and potential applications. *Nat. Rev. Mater.* **2**, 17031. https://doi.org/10.1038/natrevmats.2017.31 (2017).
10. Zhang, X. *et al.* Skyrmion-electronics: Writing, deleting, reading and processing magnetic skyrmions toward spintronic applications. *J. Phys. Condens. Matter* **32**, 143001. https://doi.org/10.1088/1361-648x/ab5488 (2020).
11. Back, C. *et al.* The 2020 skyrmionics roadmap. *J. Phys. D Appl. Phys.* **53**, 363001. https://doi.org/10.1088/1361-6463/ab8418 (2020).
12. Hayami, S. & Motome, Y. Topological spin crystals by itinerant frustration. arXiv:2103.10647 (2021).
13. Lee, M., Kang, W., Onose, Y., Tokura, Y. & Ong, N. P. Unusual Hall effect anomaly in MnSi under pressure. *Phys. Rev. Lett.* **102**, 186601. https://doi.org/10.1103/PhysRevLett.102.186601 (2009).
14. Neubauer, A. *et al.* Topological Hall effect in the *A* phase of MnSi. *Phys. Rev. Lett.* **102**, 186602. https://doi.org/10.1103/PhysRevLett.102.186602 (2009).
15. Zang, J., Mostovoy, M., Han, J. H. & Nagaosa, N. Dynamics of skyrmion crystals in metallic thin films. *Phys. Rev. Lett.* **107**, 136804. https://doi.org/10.1103/PhysRevLett.107.136804 (2011).
16. Iwasaki, J., Mochizuki, M. & Nagaosa, N. Universal current-velocity relation of skyrmion motion in chiral magnets. *Nat. Commun.* **4**, 1463. https://doi.org/10.1038/ncomms2442 (2013).
17. Dzyaloshinsky, I. A thermodynamic theory of "weak" ferromagnetism of antiferromagnetics. *J. Phys. Chem. Solids* **4**, 241–255. https://doi.org/10.1016/0022-3697(58)90076-3 (1958).
18. Moriya, T. Anisotropic superexchange interaction and weak ferromagnetism. *Phys. Rev.* **120**, 91–98. https://doi.org/10.1103/PhysRev.120.91 (1960).
19. Binz, B., Vishwanath, A. & Aji, V. Theory of the helical spin crystal: a candidate for the partially ordered state of MnSi. *Phys. Rev. Lett.* **96**, 207202. https://doi.org/10.1103/PhysRevLett.96.207202 (2006).
20. Okubo, T., Chung, S. & Kawamura, H. Multiple-q states and the skyrmion lattice of the triangular-lattice Heisenberg antiferromagnet under magnetic fields. *Phys. Rev. Lett.* **108**, 017206. https://doi.org/10.1103/PhysRevLett.108.017206 (2012).
21. Leonov, A. O. & Mostovoy, M. Multiply periodic states and isolated skyrmions in an anisotropic frustrated magnet. *Nat. Commun.* **6**, 8275. https://doi.org/10.1038/ncomms9275 (2015).
22. Batista, C. D., Lin, S.-Z., Hayami, S. & Kamiya, Y. Frustration and chiral orderings in correlated electron systems. *Rep. Prog. Phys.* **79**, 084504. https://doi.org/10.1088/0034-4885/79/8/084504 (2016).
23. Ozawa, R., Hayami, S. & Motome, Y. Zero-field skyrmions with a high topological number in itinerant magnets. *Phys. Rev. Lett.* **118**, 147205. https://doi.org/10.1103/PhysRevLett.118.147205 (2017).
24. Hayami, S., Ozawa, R. & Motome, Y. Effective bilinear-biquadratic model for noncoplanar ordering in itinerant magnets. *Phys. Rev. B* **95**, 224424. https://doi.org/10.1103/PhysRevB.95.224424 (2017).
25. Amoroso, D., Barone, P. & Picozzi, S. Spontaneous skyrmionic lattice from anisotropic symmetric exchange in a Ni-halide monolayer. *Nat. Commun.* **11**, 5784. https://doi.org/10.1038/s41467-020-19535-w (2020).
26. Zhang, X. *et al.* Skyrmion dynamics in a frustrated ferromagnetic film and current-induced helicity locking-unlocking transition. *Nat. Commun.* **8**, 1717. https://doi.org/10.1038/s41467-017-01785-w (2017).
27. Rózsa, L. *et al.* Formation and stability of metastable skyrmionic spin structures with various topologies in an ultrathin film. *Phys. Rev. B* **95**, 094423. https://doi.org/10.1103/PhysRevB.95.094423 (2017).
28. Ruderman, M. A. & Kittel, C. Indirect exchange coupling of nuclear magnetic moments by conduction electrons. *Phys. Rev.* **96**, 99–102. https://doi.org/10.1103/PhysRev.96.99 (1954).
29. Kasuya, T. A theory of metallic ferro- and antiferromagnetism on Zener's model. *Prog. Theor. Phys.* **16**, 45–57. https://doi.org/10.1143/PTP.16.45 (1956).
30. Yosida, K. Magnetic properties of Cu–Mn alloys. *Phys. Rev.* **106**, 893–898. https://doi.org/10.1103/PhysRev.106.893 (1957).
31. Hayami, S. Multiple-Q magnetism by anisotropic bilinear-biquadratic interactions in momentum space. *J. Magn. Magn. Mater.* **513**, 167181. https://doi.org/10.1016/j.jmmm.2020.167181 (2020).
32. Hayami, S. & Yambe, R. Degeneracy lifting of Néel, bloch, and anti-skyrmion crystals in centrosymmetric tetragonal systems. *J. Phys. Soc. Jpn.* **89**, 103702. https://doi.org/10.7566/JPSJ.89.103702 (2020).
33. Hayami, S. & Motome, Y. Square skyrmion crystal in centrosymmetric itinerant magnets. *Phys. Rev. B* **103**, 024439. https://doi.org/10.1103/PhysRevB.103.024439 (2021).

34. Hayami, S. & Motome, Y. Noncoplanar multiple-*q* spin textures by itinerant frustration: effects of single-ion anisotropy and bond-dependent anisotropy. *Phys. Rev. B* **103**, 054422. https://doi.org/10.1103/PhysRevB.103.054422 (2021).
35. Kathyat, D. S., Mukherjee, A. & Kumar, S. Microscopic magnetic Hamiltonian for exotic spin textures in metals. *Phys. Rev. B* **102**, 075106. https://doi.org/10.1103/PhysRevB.102.075106 (2020).
36. Kurumaji, T. *et al.* Skyrmion lattice with a giant topological Hall effect in a frustrated triangular-lattice magnet. *Science* **365**, 914–918. https://doi.org/10.1126/science.aau0968 (2019).
37. Hirschberger, M. *et al.* High-field depinned phase and planar Hall effect in the skyrmion host Gd_2PdSi_3. *Phys. Rev. B* **101**, 220401. https://doi.org/10.1103/PhysRevB.101.220401 (2020).
38. Moody, S. H. *et al.* Charge Density Waves and Coplanar Magnetism in Gd_2PdSi_3. arXiv:2010.14326 (2020).
39. Tang, F. *et al.* Crystallographic superstructure in R_2PdSi_3 compounds ($R =$ heavy rare earth). *Phys. Rev. B* **84**, 104105. https://doi.org/10.1103/PhysRevB.84.104105 (2011).
40. Schrieffer, J. R. & Wolff, P. A. Relation between the Anderson and Kondo Hamiltonians. *Phys. Rev.* **149**, 491–492. https://doi.org/10.1103/PhysRev.149.491 (1966).
41. Akagi, Y., Udagawa, M. & Motome, Y. Hidden multiple-spin interactions as an origin of spin scalar chiral order in frustrated Kondo lattice models. *Phys. Rev. Lett.* **108**, 096401. https://doi.org/10.1103/PhysRevLett.108.096401 (2012).
42. Hayami, S. & Motome, Y. Néel- and bloch-type magnetic vortices in Rashba metals. *Phys. Rev. Lett.* **121**, 137202. https://doi.org/10.1103/PhysRevLett.121.137202 (2018).
43. Okada, K. N., Kato, Y. & Motome, Y. Multiple-*q* magnetic orders in Rashba-Dresselhaus metals. *Phys. Rev. B* **98**, 224406. https://doi.org/10.1103/PhysRevB.98.224406 (2018).
44. Xia, K., Zhang, W., Lu, M. & Zhai, H. Noncollinear interlayer exchange coupling caused by interface spin-orbit interaction. *Phys. Rev. B* **55**, 12561–12565. https://doi.org/10.1103/PhysRevB.55.12561 (1997).
45. Hayami, S., Okubo, T. & Motome, Y. Phase Shift in Skyrmion Crystals. arXiv:2005.03168 (2020).
46. Chaika, A. N. *et al.* Electronic structure of R_2PdSi_3($R =$ La, Ce, Gd, and Tb) compounds. *Phys. Rev. B* **64**, 125121. https://doi.org/10.1103/PhysRevB.64.125121 (2001).
47. Inosov, D. S. *et al.* Electronic structure and nesting-driven enhancement of the RKKY interaction at the magnetic ordering propagation vector in Gd_2PdSi_3 and Tb_2PdSi_3. *Phys. Rev. Lett.* **102**, 046401. https://doi.org/10.1103/PhysRevLett.102.046401 (2009).
48. Kotsanidis, P. A., Yakinthos, J. K. & Gamari-Seale, E. Magnetic properties of the ternary rare earth silicides R_2PdSi_3 (R = Pr, Nd, Gd, Tb, Dy, Ho, Er, Tm and Y). *J. Magn. Magn. Mater.* **87**, 199. https://doi.org/10.1016/0304-8853(90)90215-C (1990).
49. Nomoto, T., Koretsune, T. & Arita, R. Formation mechanism of the helical **Q** structure in Gd-based skyrmion materials. *Phys. Rev. Lett.* **125**, 117204. https://doi.org/10.1103/PhysRevLett.125.117204 (2020).

Acknowledgements

We thank for K. Shimizu for fruitful discussions. This research was supported by JSPS KAKENHI Grants Nos. JP18K13488, JP19K03752, JP19H01834, JP21H01037, and by JST PREST (JPMJPR20L8). Parts of the numerical calculations were performed in the supercomputing systems in ISSP, the University of Tokyo.

Author contributions

R.Y. performed the calculations and S.H. supervised the project. All authors reviewed the manuscript.

Competing interests

The authors declare no competing interests.

Additional information

Supplementary Information The online version contains supplementary material available at https://doi.org/10.1038/s41598-021-90308-1.

Correspondence and requests for materials should be addressed to R.Y.

Reprints and permissions information is available at www.nature.com/reprints.

Publisher's note Springer Nature remains neutral with regard to jurisdictional claims in published maps and institutional affiliations.